Acta Pharmaceutica Sinica B 2020;10(11):2198–2211

Chinese Pharmaceutical Association
Institute of Materia Medica, Chinese Academy of Medical Sciences

Acta Pharmaceutica Sinica B

www.elsevier.com/locate/apsb
www.sciencedirect.com

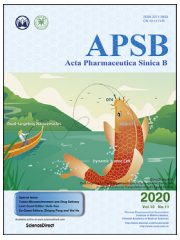

ORIGINAL ARTICLE

# Tailored core–shell dual metal–organic frameworks as a versatile nanomotor for effective synergistic antitumor therapy

**Biyuan Wu[a], Jintao Fu[a], Yixian Zhou[a], Sulan Luo[a], Yiting Zhao[a], Guilan Quan[b,*], Xin Pan[a,*], Chuanbin Wu[a,b]**

[a]*School of Pharmaceutical Sciences, Sun Yat-sen University, Guangzhou 510006, China*
[b]*College of Pharmacy, Jinan University, Guangzhou 510632, China*

Received 11 April 2020; received in revised form 5 June 2020; accepted 28 June 2020

**KEY WORDS**

Metal–organic frameworks;
Core–shell structure;
Synergistic therapy;
Photothermal therapy;
Photodynamic therapy;
Fenton-like reaction

**Abstract** Malignant tumor has become an urgent threat to global public healthcare. Because of the heterogeneity of tumor, single therapy presents great limitations while synergistic therapy is arousing much attention, which shows desperate need of intelligent carrier for co-delivery. A core–shell dual metal–organic frameworks (MOFs) system was delicately designed in this study, which not only possessed the unique properties of both materials, but also provided two individual specific functional zones for co-drug delivery. Photosensitizer indocyanine green (ICG) and chemotherapeutic agent doxorubicin (DOX) were stepwisely encapsulated into the nanopores of MIL-88 core and ZIF-8 shell to construct a synergistic photothermal/photodynamic/chemotherapy nanoplatform. Except for efficient drug delivery, the MIL-88 could be functioned as a nanomotor to convert the excessive hydrogen peroxide at tumor microenvironment into adequate oxygen for photodynamic therapy. The DOX release from MIL-88-ICG@ZIF-8-DOX nanoparticles was triggered at tumor acidic microenvironment and further accelerated by near-infrared (NIR) light irradiation. The *in vivo* antitumor study showed superior synergistic antitumor effect by concentrating the nanoparticles into dissolving microneedles as compared to intravenous and intratumoral injection of nanoparticles, with a significantly higher inhibition rate. It is anticipated that the multi-model synergistic system based on dual-MOFs was promising for further biomedical application.

*Corresponding authors.
E-mail addresses: xiaoplanet@163.com (Guilan Quan), panxin2@mail.sysu.edu.cn (Xin Pan).

Peer review under responsibility of Chinese Pharmaceutical Association and Institute of Materia Medica, Chinese Academy of Medical Sciences.

https://doi.org/10.1016/j.apsb.2020.07.025

## 1. Introduction

Malignant tumor has been the leading cause to the global death with an estimation of 18.1 million new cancer cases and 9.6 million cancer deaths in 2018[1]. It is urgent to develop effective therapeutic strategies to inhibit the rapid growth of cancer mortality. Conventional treatments including chemotherapy, radiotherapy, and surgery have inevitable limitations, such as systemic side effects, high recurrence rate, and low therapeutic efficacy[2,3]. Recently, external micro-energy has emerged as potential tool with improved tumoricidal effect[4–7]. Among them, phototherapy including photothermal therapy (PTT) and photodynamic therapy (PDT) has aroused increasing attention due to its unique properties including high selectivity, low systemic toxicity, and limited therapeutic resistance, which utilizes photosensitizer accumulated at the tumor tissue to kill cancer cells by effectively converting the near-infrared (NIR) light energy into heat or reactive oxygen species (ROS). On the consideration of the specificity, diversity, and heterogeneity of tumor, single therapy can hardly achieve ideal therapeutic outcome. By contrast, combinational therapy based on different mechanisms usually presents synergic antitumor effect, such as PTT/PDT, PDT/chemotherapy, and PTT/chemotherapy[8–10]. Co-encapsulation of different drugs in suitable drug delivery system is the prerequisite for synergic therapy. However, carrier applied for effective and intelligent co-delivery still remains a great challenge, which severely limited the development of high-efficient combinational system.

Previous researches about multi-antitumor drug delivery were mainly classified into two strategies[11]. One is the self-assembly strategy by directly conjugating therapeutic drugs with other active molecules[12,13]. Nevertheless, the active ingredients may be interfered mutually during the storage or suffered from premature release before reaching the target tissue. And the other one is encapsulating all therapeutic agents into the matrix or surface of nanocarriers[14–16]. However, the surface modification limitation and uncontrollable encapsulation may limit the combinational drug delivery. Therefore, an ideal co-delivery system should provide the opportunity to simultaneously load different drugs at individual compartments without mutual interference. Moreover, the system can be further designed with functional modification. A promising methodology to meet these requirements was heterogeneous hybridization, which can integrate the advantages of different carriers and subsequently endow the hybrid carrier with novel chemical and physical properties. Metal–organic frameworks (MOFs) were an emerging class of hybrid porous materials based on coordination bonds between metal ions (or clusters) and organic ligands[17,18]. With huge surface area and ordered porous interior, the MOFs can be used as versatile host to encapsulate a large amount of biological agents, and subsequently stabilize the guest molecules by their spatial confinement. Through judicious choice of organic and inorganic components, the crystalline structure and chemical functionalities of MOFs can be deliberately modulated[19].

Especially, MIL series and ZIF series are two representative subclasses of MOFs. MIL-88, consisted of ferric ions and 2-aminoterephthalic acid (BDC-$NH_2$), shows excellent framework flexibility since its unit cell can reversibly swell and shrink without harming the framework topology, which is called breathing behavior[20,21]. With this unique property, the carrier can intelligently adapt its pore to the dimension of drugs and subsequently stabilize the sensitive drugs[22]. Besides, MIL-88 carrier itself can also be functioned as a nanomotor to provide continuous oxygen supply, which is the prerequisite for efficient PDT. It is worth noting that the typical characteristics of the tumor microenvironment are lack of oxygen, weak acidity (pH 4.5–7.0), and excessive hydrogen peroxide[23]. The ferric ions in MIL-88 endow the carrier enzyme-like activity, which can trigger Fenton-like reaction with excessive hydrogen peroxide in tumor microenvironment to generate oxygen[24–26]. ZIF-8, composed of zinc ions and 2-methyl imidazole (2-MeIM), shows great stability in physiological environment but gradually degrades at acidic condition. The intelligent pH-sensitive property can avoid premature drug leakage and realize site-specific release in response to the acidic tumor microenvironment. Therefore, we hypothesized that the dual MOFs hybridized from MIL-88 and ZIF-8 could not only possess the unique properties of both materials, but also provide two special functional zones for combinational drug delivery.

In this study, a core–shell dual MOFs was constructed using MIL-88 as internal core and ZIF-8 as external shell, which was expected to be employed as a versatile nanoplatform for synergistic photothermal/photodynamic/chemotherapy of tumor (Scheme 1). Indocyanine green (ICG), a photosensitizer approved by U.S. Food and Drug Administration (FDA), was encapsulated into internal MIL-88 by impregnation method. Compared with the previous ICG delivery system based on MOFs, the MIL-88 was expected to further improve ICG stability, avoiding from rapid aggregation and photo-degradation due to the breathing behavior[27,28]. And the chemotherapeutic agent doxorubicin (DOX) was loaded into the ZIF-8 shell. After irradiation, the ICG could convert the light energy into heat or ROS to kill tumor cells. The site- and time-specific controlled drug release profile could be realized since the degradation of ZIF-8 could be triggered by acidic tumor microenvironment and the high temperature induced by PTT. Additionally, the MIL-88 was functioned as an intrinsic oxygen producer *via* Fenton-like reaction, generating continuous oxygen to strengthen the PDT efficacy. In comparison with traditional co-delivery system, this multifunctional core–shell dual MOFs based on MIL-88 and ZIF-8 served as not only drug loading platform with two separate delivery zones, but also a releasing switch and self-stimulated oxygen producer.

The successful synthesis of MIL-88-ICG@ZIF-8-DOX was confirmed by scanning electron microscope (SEM), energy-dispersive X-ray spectroscopy (EDX), and powder X-ray diffraction (PXRD). The *in vitro* drug release study confirmed that DOX release could be triggered by low pH value and NIR irradiation. Microneedles are emerging as a novel transdermal administration strategy, which can directly deliver drugs to the target tissue

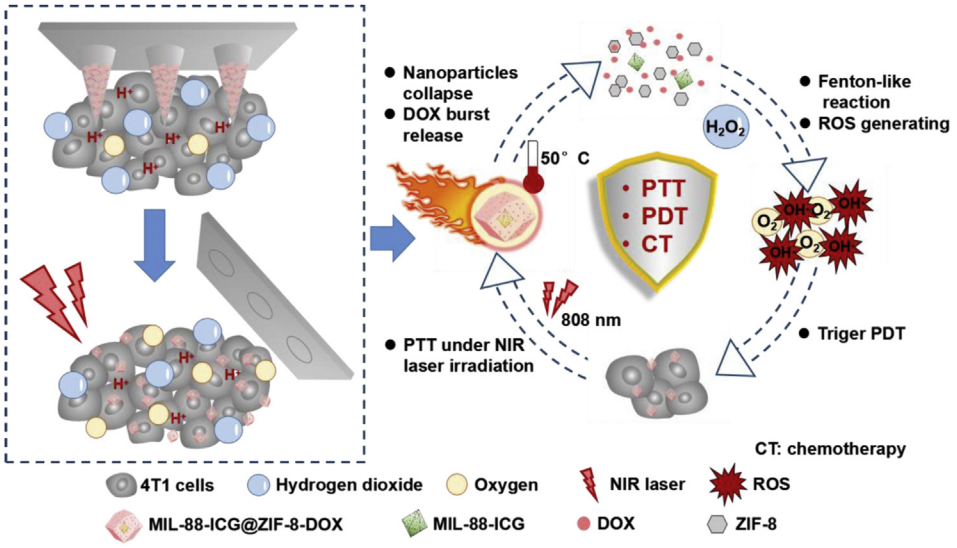


**Scheme 1** Schematic illustration of MIL-88-ICG@ZIF-8-DOX nanoparticles for synergistic photothermal/photodynamic/chemotherapy of tumor.

without systematic circulation. Therefore, the nanoparticles were loaded into dissolving microneedles for subcutaneous tumor model therapy to further evaluate the *in vivo* tumoricidal activity. It is anticipated that the multi-model synergistic system based on core–shell dual-MOFs is promising for further biomedical application.

## 2. Materials and methods

### 2.1. Materials

Ferric chloride hexahydrate ($FeCl_3 \cdot 6H_2O$, 98%), BDC–$NH_2$, 2-MeIM, DOX, ICG, and *N*,*N*-dimethylformamide (DMF) were obtained from Aladdin Bio-Chem Technology Co., Ltd. (Shanghai, China). Zinc nitrate hexahydrate [$Zn(NO_3)_2 \cdot 6H_2O$] was provided by Meryer Chemical Technology Co., Ltd. (Shanghai, China). Methanol (Analytical reagent, >99.7%) was purchased from Tianjin Kemiou Chemical Reagent Co., Ltd. (Tianjin, China). CCK-8 was acquired from Dojindo Laboratories (Kumamoto, Japan). Annexin V-FITC/PI was obtained from Shanghai Yishan Biotechnology Co., Ltd. (Shanghai, China). 4′,6-Diamidino-2-phenylindole (DAPI) was purchased from Beijing Solarbio Science & Technology Co., Ltd. (Beijing, China).

### 2.2. Synthesis of MIL-88 nanoparticles

MIL-88 nanoparticles were synthesized according to the previous reports[29]. Briefly, 0.126 g of BDC–$NH_2$ and 0.187 g of $FeCl_3 \cdot 6H_2O$ were dissolved in 15 mL of DMF, followed by adding 3.45 mmol of acetic acid. The resulting mixture was placed in an oil bath at 120 °C for 4 h. Afterwards, the brown product was cooled to room temperature, collected by centrifugation, and further washed several times with methanol to remove excess reactants.

### 2.3. Preparation of MIL-88-ICG

The ICG loading was performed by impregnation method. Briefly, the mixture suspension containing ICG and MIL-88 nanoparticles was stirred at 300 rpm on the magnetic stirrer (WH-610D, Wiggens, Berlin, Germany) overnight to reach absorption equilibrium. Then, the MIL-88-ICG nanoparticles were collected and washed three times with methanol to remove the ICG molecules attached on the surface of nanoparticles.

### 2.4. Synthesis of MIL-88-ICG@ZIF-8

Ten milligram of MIL-88-ICG nanoparticles were mixed with 640 mg of $Zn(NO_3)_2 \cdot 6H_2O$ and 640 mg of 2-MeIM by stirring at 500 rpm on the magnetic stirrer (WH-610D, Wiggens) for 1 h. Then, the obtained composites were collected and washed three times with methanol.

### 2.5. Preparation of MIL-88-ICG@ZIF-8-DOX

The DOX was also loaded into the pores of ZIF-8 shell by impregnation method. After continuously stirring overnight, the excess DOX in the supernatant was collected. The encapsulation efficiency (EE) and drug loading (DL) of ICG and DOX was calculated using the following Eqs. (1) and (2):

$$EE(\%) = (M_1 - M_2) / M_1 \times 100 \quad (1)$$

$$DL(\%) = (M_1 - M_2) / M_3 \times 100 \quad (2)$$

where $M_1$, $M_2$, and $M_3$ represented the total amount of ICG or DOX initially fed for loading, the amount of ICG or DOX remaining in the supernatant, and the total amount of nanoparticles MIL-88-ICG@ZIF-8-DOX, respectively.

### 2.6. Characterization of MIL-88-ICG@ZIF-8-DOX

The morphology of MIL-88-ICG@ZIF-8-DOX was observed by SEM (JSM-6330F, Japanese Electronics Co., Ltd., Akashima, Japan). The samples were placed on a brass stub and then sputter-coated with gold for two cycles before examination. The nitrogen absorption−desorption isotherm of the samples, as well as pore size distribution were measured using automatic volumetric sorption analyzer (ASAP2460, Micromeritics Instrument Corp.,

Atlant, USA). The crystalline structure was evaluated by PXRD (D8 Advance, Bruker, Karlsruhe, Germany) using Cu K$\alpha$ radiation with $2\theta$ in the range of 3°−40° at a scanning rate of 5°/min. The molecular interaction was investigated by Fourier transform infrared spectroscopy (FT-IR, STA449F3/Nicolet 6700, Thermo Electron Corporation, Waltham, USA).

### 2.7. Photothermal effect of MIL-88-ICG@ZIF-8-DOX

MIL-88-ICG@ZIF-8-DOX aqueous suspensions (0.5, 1.0, and 2.0 mg/mL) were irradiated under 808 nm laser light. The temperature was recorded for 5 min with 30 s intervals using an infrared thermal sensing and imaging equipment (TiS75, Fluke, Everett, USA). To investigate the photostability of ICG, the MIL-88-ICG@ZIF-8-DOX aqueous suspension and pure ICG solution were exposed to NIR light for four cycles. Each cycle consisted of 5 min irradiation followed by nearly 15 min for cooling down.

### 2.8. Oxygen generation of MIL-88-ICG@ZIF-8-DOX

MIL-88-ICG@ZIF-8-DOX nanoparticles were dispersed in hydrogen peroxide (20 mmol/L) solution. The real-time production of oxygen was measured *via* an oxygen dissolving meter (JPSJ-605F, Shanghai INESA Scientific Instrument Co., Ltd., Shanghai, China).

### 2.9. Stability investigation of MIL-88-ICG@ZIF-8-DOX

MIL-88-ICG@ZIF-8-DOX, free ICG, and free DOX were dispersed into 2 mL of aqueous solution, respectively. The initial fluorescent intensity of all the samples were recorded and then kept at 4, 25, and 37 °C to investigate the influence of temperature on the stability of fluorescent cargos. The corresponding fluorescent intensity was recorded at Days 1, 3, 5, and 7, respectively.

### 2.10. Release profile of DOX

To investigate the DOX release profile, the MIL-88-ICG@ZIF-8-DOX was immersed in 6 mL of PBS solution with various pH values (pH 5.0, 6.0 and 7.4) at 37 °C with or without 808 nm laser irradiation. At different time points, 1.0 mL of supernatant was withdrawn and an equal volume of fresh medium was added. The DOX amount was determined by fluorescent spectroscopy. Each test was performed in triplicate.

### 2.11. Cellular uptake

The 4T1 cells were seeded in an NUNC™ imaging 24-well plate and pre-cultured for 24 h at 37 °C. The medium was replaced by fresh medium containing nanoparticles. After 1, 2, or 4 h of incubation, the cells were washed three times with cold PBS solution and fixed with 4% paraformaldehyde at 4 °C for 15 min. Subsequently, the cells were washed with PBS solution and stained by DAPI. Finally, the stained samples were observed by FV3000 Olympus confocal microscope.

Besides, the quantitative cellular uptake study was carried out by flow cytometry (Guava easyCyte, Merck KGaA, Darmstadt, German). Similarly, the 4T1 cells were treated as described above. After incubation with samples for different time, the cells were washed three times with cold PBS solution, harvested by trypsinization, and then collected by centrifugation. The cells were resuspended by fresh medium and analyzed by flow cytometry.

### 2.12. Detection of intracellular ROS

2′,7′-Dichlorofluorescin diacetate (DCFH-DA) was selected as the probe for detecting the intracellular ROS generation. In brief, 4T1 cells were seeded in an NUNC™ imaging 24-well plate and pre-cultured for 24 h at 37 °C. Then nanoparticles were added into the wells for 4 h of incubation at 37 °C. As for the NIR-treated group, the cells were exposed to 808 nm laser (1 W/cm$^2$) for 5 min. After removing the culture medium, the cells were washed by PBS solution for three times and further incubated in the dark with DCFH-DA (5 mmol/L) for 15 min at 37 °C. Finally, the cells were washed with PBS solution to remove excess probe for confocal microscope observation.

### 2.13. In vitro cytotoxicity assay

The 4T1 cells were seeded into the 96-well plates and incubated at 37 °C for 24 h. The original medium was replaced by fresh medium containing different concentrations of samples. For NIR-treated groups (MIL-88-ICG@ZIF-8 + NIR and MIL-88-ICG@ZIF-8-DOX + NIR), the cells were exposed to NIR light 4 h post treatment (808 nm, 1 W/cm$^2$, 5 min). Cytotoxicity was assessed at 48 h post treatment with a standard CCK-8 method, and the optical density (OD) value of each well was measured at 450 nm by a microplate reader. The relative viability was calculated by the following Eq. (3):

$$\text{Cell viability}(\%) = \text{OD}_{\text{Sample}}/\text{OD}_{\text{Control}} \times 100 \quad (3)$$

### 2.14. Live/dead cell staining assay

The 4T1 cells were seeded in 6-well plates and further treated with pre-determined groups. For NIR-treated groups (MIL-88-ICG@ZIF-8 + NIR and MIL-88-ICG@ZIF-8-DOX + NIR), the cells were exposed to NIR light 4 h post treatment (808 nm, 1 W/cm$^2$, 5 min). After incubation for 48 h, the cells were washed three times with PBS solution, stained with calcein-AM/propidium iodide (PI) kit and further incubated for another 30 min before analyzed by the cell imager.

### 2.15. Cell apoptosis measurement

The cell apoptosis measurement against 4T1 cells was investigated using flow cytometry after Annexin V-FITC and PI co-staining. Briefly, 4T1 cells were seeded in a 6-well pate and pre-cultured for 24 h at 37 °C. The medium was disposed and the cells were incubated with various samples. The NIR-treated groups were exposed to laser 4 h post administration. After further culture for 4 h, the cells were harvested, further disposed with the operation instructions of kits, and analyzed *via* flow cytometry.

### 2.16. Fabrication and characterization of nanoparticles encapsulated microneedles

The microneedles (MNs) were fabricated according to the traditional micro-molding strategy[30,31]. Briefly, the needle matrix solution was prepared by mixing hyaluronic acid (HA) solution and nanoparticle suspension at a fixed ratio of 1:2 (*v/v*). The obtained mixture was poured over the female mold and centrifuged at 4000 rpm (DL-400B, Shanghai Anting Scientific Instrument Factory, Shanghai, China) for 5 min to fill the needle cavities. After removing the excess needle solution, the base solution (10 g of PVP K90 was dissolved in 3.2 mL of ethyl alcohol) was added to the female mold, followed by centrifugation at 3500 rpm (DL-400B, Shanghai Anting Scientific Instrument Factory) for another 3 min. Then, the MNs with 800 μm in height were dried at room temperature for 12 h before peeled out of the female mold.

The morphology of MNs was observed *via* digital camera and SEM. Besides, the nanoparticle distribution in the MNs patch was analyzed *via* confocal laser scanning microscope (CLSM).

### 2.17. Skin insertion study of MNs

A piece of MIL-88-ICG@ZIF-8-DOX-loaded MNs patch was pressed onto the surface of rat skin for 1 min. After removing the patch, the pierced skin was stained by trypan blue solution (0.4%, *w/v*) for 5 min to observe the pores retained on the skin surface. In addition, hematoxylin and eosin (H&E) staining, optical coherence tomography (OCT), and CLSM were also used to observe the penetration ability of MNs.

### 2.18. In vivo antitumor study

All animal experiments in this research were approved and supervised by the Animal Ethics Committee of Sun Yat-sen University, China. The female BALB/c animals (5−8 weeks) were obtained from Sun Yat-sen University Laboratory Animal Center (Guangzhou, China) and supplied with sufficient food and water. The tumor bearing mice were obtained by subcutaneous injection 4T1 cells ($1 \times 10^7$ cells) into the pre-shaved back. When the tumor volume reached approximately 100 $mm^3$, the mice were randomly divided into 8 groups (6 mice per group) and subjected to the following treatments: (1) control group (Control), (2) intravenous injection of MIL-88-ICG@ZIF-8-DOX + NIR (i.v.+NIR), (3) intratumoral injection of MIL-88-ICG@ZIF-8-DOX + NIR (i.t.+NIR), (4) MIL-88@ZIF-8-DOX@MNs (D@MNs), (5) MIL-88-ICG@ZIF-8@MNs + NIR (I@MNs + NIR), (6) MIL-88-ICG@ZIF-8-DOX@MNs (ID@MNs), (7) MIL-88-ICG@ZIF-8-DOX@MNs + NIR (ID@MNs + NIR), (8) two patches of MIL-88-ICG@ZIF-8-DOX@MNs + NIR (Two-ID@MNs + NIR). The tumor size was recorded every 2 days by a caliper and the volume was calculated according to Eq. (4):

$$V = W^2 L/2 \tag{4}$$

in which $W$ and $L$ were the shortest and longest diameter, respectively. After observation for 20 days, all the mice were sacrificed and the blood was gathered for blood routine examination. Besides, the major organs and tumors were collected for further analysis.

### 2.19. Pathological investigation

The collected tissues of treated mice were fixed in 4% paraformaldehyde and then imbedded in paraffin block. Subsequently, the samples were sectioned for different tests. (1) The major organs and tumors were stained with H&E. (2) As for Ki-67 staining, tumor sections were incubated with anti-Ki-67 antibody overnight at 4 °C. (3) For apoptosis analysis, TUNEL kit was used to stain tumor sections.

### 2.20. Statistical analysis

Statistical analysis was performed using a one-way ANOVA (SPSS 13.0) (International Business Machines Corporation, Armonk, NY, USA). The *post hoc* comparisons of the means of individual groups were performed using least significant difference test. Differences were considered significant if $P < 0.05$.

## 3. Results and discussion

### 3.1. Synthesis and characterization of MIL-88-ICG@ZIF-8-DOX

The fabrication process of core–shell dual MOFs co-delivery system was illustrated in Fig. 1A, and both ICG and DOX were encapsulated into the pores of MIL-88 and ZIF-8 by impregnation method, respectively. Firstly, MIL-88 core was prepared according to the previous literature without further modification[29]. ICG was encapsulated into the pores of MIL-88 (MIL-88-ICG) *via* electrostatic interaction, $\pi-\pi$ conjugative effect, and hydrogen−bond interaction. Then, MIL-88-ICG was acted as the crystal nucleus to attract the lattice unit of ZIF-8 accumulated over MIL-88-ICG and subsequently formed the external ZIF-8 shell. The covalent interaction between amidogen of MIL-88 or sulfonic acid group of ICG and zinc metal cluster might contribute to the initial accumulation of ZIF-8[14,32]. Finally, DOX was loaded to the pores of ZIF-8 by impregnation method (MIL-88-ICG@ZIF-8-DOX). The encapsulation efficiency of ICG and DOX in the nanoparticles was confirmed by fluorescent spectrum as 88.96% and 87.84%, respectively. Additionally, the corresponding drug loading capacity was 3.58% and 21.69%.

The as-synthesized MIL-88 appeared as octahedron shape with narrow particle size distribution of approximately 100 nm (Supporting Information Fig. S1). The nitrogen adsorption−desorption isotherm of MIL-88 exhibited type IV with an apparent hysteresis hoop (Fig. 1B). The corresponding pore size was measured as 1.3 nm (Fig. 1C). After ZIF-8 coating, MIL-88@ZIF-8 presented type I isotherm pattern with pore size of 1.0 nm due to the relatively small pore size of ZIF-8. In contrast, there is an increase both in BET surface area (from 242.02 to 865.12 $m^2/g$) and pore volume (from 0.45 to 0.58 $cm^3/g$) after ZIF-8 coating, indicating that the core–shell dual MOFs could be served as versatile reservoir for sufficient drug loading.

PXRD was used to characterize the drug loaded samples by examining the change of crystal structure and crystallinity. As shown in Fig. 1D, MIL-88 presented characteristic peaks at $2\theta$ of 9.2, 10.5, 13.5, 17.4, 18.2, and 20.28 even after ICG encapsulation[33]. The PXRD results of MIL-88-ICG@ZIF-8 matched the crystalline patterns of ZIF-8[34,35], indicating the successful formation of ZIF-8 shell. No obvious diffraction peaks of both ICG and DOX were observed in MIL-88-ICG@ZIF-8-DOX, reflecting

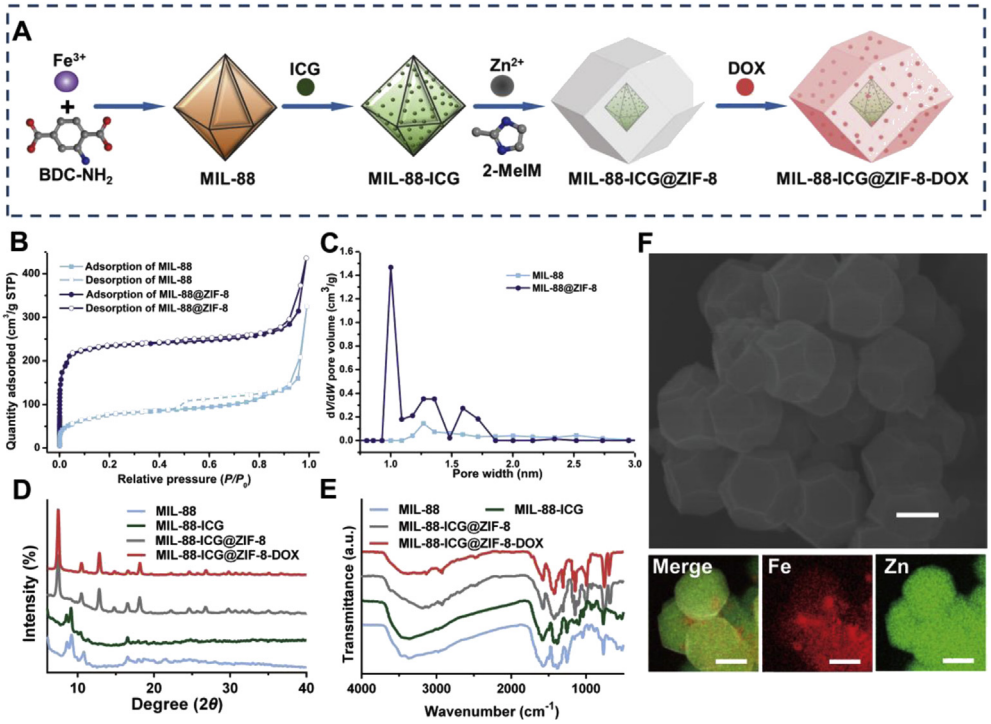


**Figure 1** (A) Schematic illustration of the synthesis process of MIL-88-ICG@ZIF-8-DOX (B) Nitrogen adsorption−desorption isotherm and (C) pore size distribution of MIL-88 and MIL-88@ZIF-8, respectively (D) PXRD patterns and (E) FT-IR spectra of MIL-88, MIL-88-ICG, MIL-88-ICG@ZIF-8, and MIL-88-ICG@ZIF-8-DOX, respectively (F) SEM and EDX images of MIL-88-ICG@ZIF-8-DOX (scale bar: 300 nm).

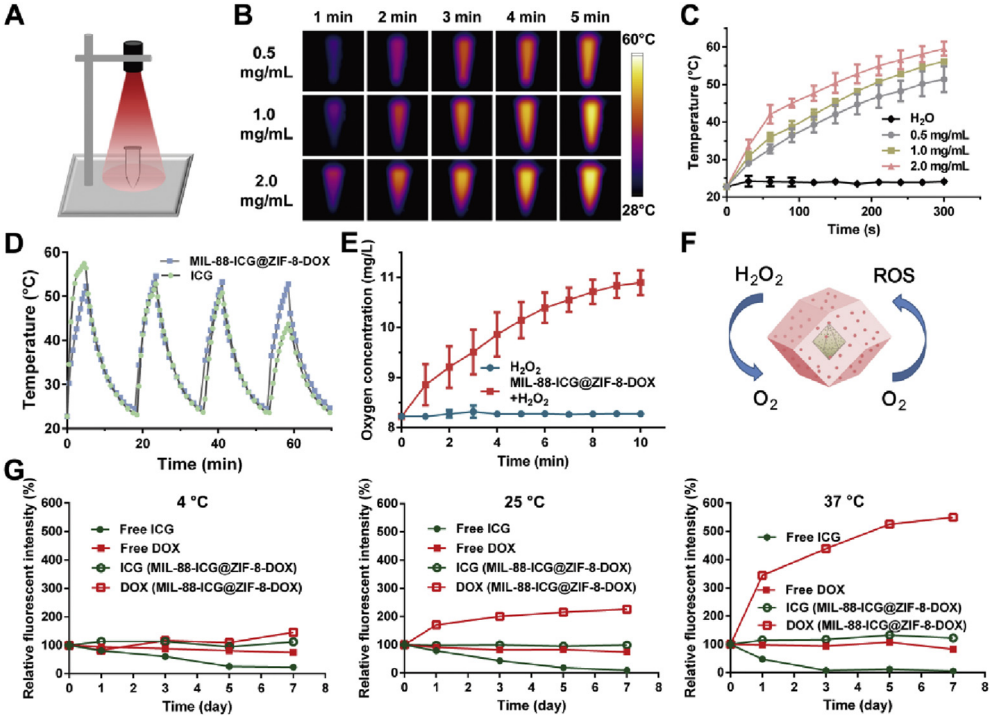


**Figure 2** (A) Schematic illustration of the *in vitro* photothermal study (B) The thermographic images of MIL-88-ICG@ZIF-8-DOX aqueous suspension under NIR irradiation for different time (C) Local temperature change curve of MIL-88-ICG@ZIF-8-DOX aqueous suspension at different time points (mean ± SD, $n = 3$) (D) Photothermal conversion curves of free ICG and MIL-88-ICG@ZIF-8-DOX for four cycles (E) Oxygen generation of MIL-88-ICG@ZIF-8-DOX in hydrogen peroxide solution (mean ± SD, $n = 3$) (F) Schematic illustration of oxygen generation and ROS production (G) Fluorescent stability of free cargo and MIL-88-ICG@ZIF-8-DOX in aqueous suspension at different temperatures for a week.

that drugs in the pores of carriers were in an amorphous or molecular dispersion state. Furthermore, the molecular structure and interaction were determined by FT-IR in Fig. 1E. Typical absorption bands of ZIF-8 at 1580, 1150, and 422 $cm^{-1}$ were observed in the sample of MIL-88-ICG@ZIF-8, reflecting the existence of ZIF-8 on the surface of MIL-88-ICG. The successful synthesis of MIL-88-ICG@ZIF-8-DOX was further confirmed by SEM and EDX in Fig. 1F. Evidently, the element Zn was homogenously distributed throughout the whole nanostructure, while the element Fe was embedded into the inner core of nanoparticles, which confirmed that ZIF-8 has been successfully covered around the MIL-88 core.

### 3.2. *The in vitro photothermal effect and oxygen generation profile of MIL-88-ICG@ZIF-8-DOX*

To evaluate the photothermal efficacy of MIL-88-ICG@ZIF-8-DOX, the nanoparticle suspension at various concentrations was exposed to NIR laser for 5 min (Fig. 2A) and the corresponding temperature was recorded by an infrared thermal sensing and imaging equipment. As exhibited in Fig. 2B and C, the temperature of MIL-88-ICG@ZIF-8-DOX suspension (0.5 mg/mL) quickly increased to 51.3 °C, whereas the blank medium just kept constant. Moreover, the concentration-dependent photothermal effect was observed when the concentration of nanoparticles increased from 0.5 to 2.0 mg/mL. Furthermore, the photothermal stability of MIL-88-ICG@ZIF-8-DOX was investigated in comparison with pure ICG solution. Both nanoparticle suspension and pure ICG solution were irradiated by NIR laser and cooled to room temperature for several cycles. As displayed in Fig. 2D, the photothermal conversion ability of MIL-88-ICG@ZIF-8-DOX presented negligible change after four cycles. By contrast, a continuous decline of the highest temperature was observed in the group of ICG, which probably related to the serious photobleaching of ICG after laser irradiation[36].

In order to investigate the oxygen generation ability of MIL-88-ICG@ZIF-8-DOX, nanoparticles were suspended in hydrogen peroxide solution and the real-time oxygen concentration was recorded by oxygen dissolving meter (Fig. 2E and F). Contrast to constant oxygen level in control group (hydrogen peroxide solution), a strong increasing oxygen signal was detected in nanoparticle suspension. This revealed that the Fenton-like reaction between MIL-88-ICG@ZIF-8-DOX and hydrogen peroxide triggered the production of oxygen.

Except for the remarkable ability to produce heat and oxygen, the protective ability for cargos was also verified in various temperatures. As shown in Fig. 2G, obvious fluorescence decline was determined in the group of free ICG and the tendency sped up as the temperature increased. By contrast, ICG loaded in the nanoparticles presented remarkable fluorescent stability with negligible fluorescence quenching. The detectable fluorescence intensity of DOX in the system increased as the experimental temperature and incubation time increased. It has been found that the DOX could chelate with MOFs, which lead to the decreased fluorescence[37]. High temperature might be beneficial for the break of coordination bond between DOX and zinc ions to recover the fluorescence of DOX.

### 3.3. *Drug release properties of MIL-88-ICG@ZIF-8-DOX*

Inspired by the pH-sensitive property of ZIF-8 material[38,39], the release profiles of DOX at different pH values (pH = 5.0, 6.0 and 7.4) were tested. As exhibited in Fig. 3A, the cumulative release amount of DOX increased with the reduction of pH value. In particular, approximately 60% and 25% DOX released in pH 5.0 and 7.4 after 12 h, respectively, which could be ascribed to the framework decomposition under acidic condition. Moreover, the break of the coordinate bonds between DOX and zinc ions at lower pH might also contributes to the fast release. Fig. 3B presented the release profile triggered by repeated NIR irradiation, where laser-on step induced a steep increase in DOX release in comparison with that without NIR irradiation in the identical pH (Fig. 3A). The accelerated DOX release was probably associated with the dissociation of carriers induced by the thermal expansion. The speculation about the mechanism of drug release from MIL-88-ICG@ZIF-8-DOX was presented in Fig. 3C. The framework corrosion under acidic condition was the main cause for DOX release without NIR irradiation, while framework dissociation under NIR irradiation could accelerate the collapse process, which increased the contact surface between DOX-loaded fractions and medium. Because of the weak acidic tumor microenvironment, the results above indicated that the nanoparticles could realize time and site-specific control drug release.

The cellular uptake and intracellular release behaviors of MIL-88-ICG@ZIF-8-DOX were investigated by culturing 4T1 cells with nanoparticles and observed through CLSM at different time points. As expected in Fig. 3D and E and Supporting Information Fig. S2, the intensity of intracellular DOX signal became stronger and gradually distributed into the nucleus as the incubation time increased, implying that the MIL-88-ICG@ZIF-8-DOX was internalized continuously. Comparatively, the fluorescence of ICG was accumulated in the cytoplasm. The fluorescence separation between ICG and DOX might be ascribed to the disintegration of MIL-88-ICG@ZIF-8-DOX in the acidic cellular environment, such as lysosome, where the external shell (ZIF-8-DOX) could disintegrate slowly, further inducing the core structure collapse and release free cargo stepwisely.

### 3.4. *In vitro cytotoxicity of MIL-88-ICG@ZIF-8-DOX against 4T1 cells*

It has been found that the tumor microenvironment is lack of oxygen, which hindered efficient PDT treatment. In this study, MIL-88 has been confirmed as a nanomotor for continuous oxygen supply. To detect the intracellular ROS generation, DCFH-DA was utilized as sensor due to the sensitive oxidation capacity to emit green fluorescence. As shown in Fig. 4A, compared with the control group, strong green fluorescence was observed in 4T1 cells treated by MIL-88-ICG@ZIF-8-DOX under irradiation for 5 min, suggesting the generation of ROS. In addition, less green fluorescence was also exhibited in MIL-88-ICG@ZIF-8-DOX group without NIR irradiation, which might be related to the ROS induced by zinc ions released from the frameworks *via* Fenton-like reaction[40,41].

To verify the synergistic therapeutic effect of the photothermal/photodynamic/chemotherapy, 4T1 cells were incubated with different samples with or without NIR irradiation (Fig. 4B). Cells exposed to NIR irradiation were not inhibited. Besides, the treatment with MIL-88@ZIF-8 and MIL-88-ICG@ZIF-8 did not affect the growth of 4T1 cells. These results indicated that both the NIR irradiation and the carriers were in good biocompatibility. After incubated with MIL-88@ZIF-8-DOX and MIL-88-ICG@ZIF-8-DOX, the cell viabilities decreased as the concentration of DOX increased. Comparatively, the cell viability steeply

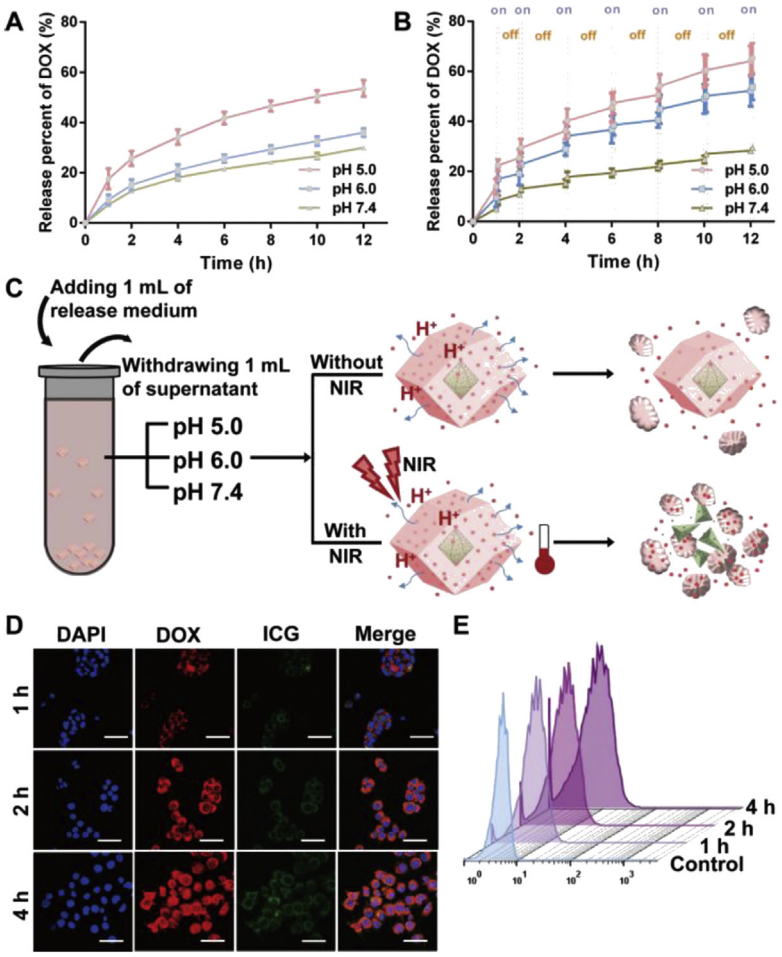


**Figure 3** (A) DOX release profiles from MIL-88-ICG@ZIF-8-DOX in the buffer solution with different pH values (mean ± SD, $n = 3$) (B) DOX release profiles from MIL-88-ICG@ZIF-8-DOX under on/off NIR irradiation cycles (mean ± SD, $n = 3$) (C) The speculation about the drug release mechanisms of MIL-88-ICG@ZIF-8-DOX (D) CLSM images and (E) flow cytometric analysis of 4T1 cells incubated with MIL-88-ICG@ZIF-8-DOX for 1, 2, and 4 h, respectively (scale bar: 50 μm).

reduced to 6.9% when the cells were treated with MIL-88-ICG@ZIF-8-DOX under NIR irradiation even the concentration of DOX and ICG were 0.31 and 0.06 μg/mL, respectively. The remarkable synergistic cytotoxicity could be explained that the heat energy generated by ICG under NIR irradiation might increase the cell membrane permeability and subsequently enhance the cell sensitivity to DOX. In addition, ROS produced in the cell environment also contributed to the death of cells. Calcein-AM (green fluorescence)/PI (red fluorescence) were used to stain live and dead cells, respectively. As shown in Fig. 4C, strong red fluorescence appeared in cells that cultured with MIL-88-ICG@ZIF-8-DOX + NIR, which was consistent with the results of cell viability.

For quantitatively distinguishing viable cells from apoptotic or dead cells *via* flow cytometry, the Annexin V-FITC/PI apoptosis detection kit was utilized. Q1, Q2, Q3, and Q4 represent dead cells, late apoptosis or necrosis cells, early apoptosis cells, and vital cells, respectively[42]. As shown in Supporting Information Fig. S3 and Fig. 4D, after treated with MIL-88-ICG@ZIF-8-DOX under irradiation for 5 min, the percentage of apoptosis or dead cells were 24.4% and 40.9% with the increasing dosage (25 and 50 μg/mL), respectively, which were much higher than the cells treated without NIR irradiation. Relatively, negligible apoptosis or dead cells were found in the control group. The percentage of the cells at different stages after various treatments was shown in Supporting Information Fig. S4. These results confirmed the remarkable multi-model therapeutic efficacy.

### *3.5. Preparation and characterization of MIL-88-ICG@ZIF-8-DOX-loaded MNs*

Recently, MNs patch have been emerged as an alternative strategy for efficient transdermal drug delivery. It shows great potential in intralesional delivery of antitumor nanosystem into the superficial tumors. Therefore, the MIL-88-ICG@ZIF-8-DOX nanoparticles were loaded in the MNs (MIL-88-ICG@ZIF-8-DOX@MNs) to realize high delivery efficiency, minimal invasiveness, and convenience for administration.

The fabrication process of MIL-88-ICG@ZIF-8-DOX@MNs was shown in Fig. 5A. Briefly, the nanoparticle suspension was mixed with HA to form the needle matrix solution. Additionally, the base solution was prepared by dissolving a defined amount of PVP K90 in ethanol. The obtained MNs patch (12 mm × 12 mm) consisted of 144 conical needles with 800 μm in height and 300 μm in diameter. In addition, the total cavity volume of each MNs patch was 3.5 μL. The results of SEM (Supporting

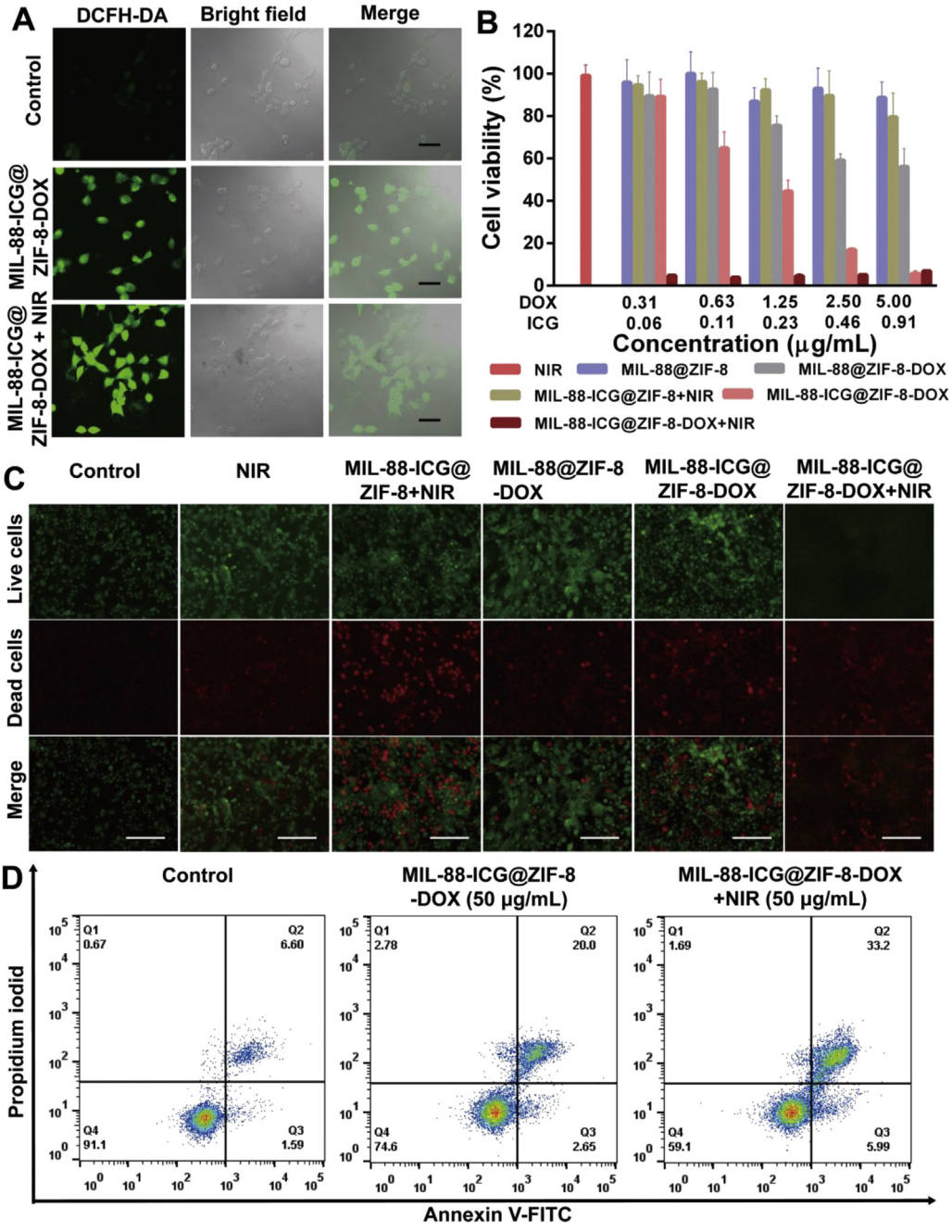


**Figure 4** (A) CLSM images of intracellular ROS generation in 4T1 cells (scale bar: 50 μm) (B) Cell viability of 4T1 cells after 48 h of incubation with various treatments (mean ± SD, $n = 6$) (C) Fluorescence images of 4T1 cells incubated with various treatments and followed by co-staining with calcein-AM/PI (scale bar: 100 μm) (D) Flow cytometric analysis of 4T1 cells incubated with nanoparticles (50 μg/mL).

Information Fig. S5) and optical microscope (Supporting Information Fig. S6) showed the morphology of MNs. Compared with the HA microneedles (without nanoparticle loading, Supporting Information Fig. S7), no deficiency and cracks were presented in the MIL-88-ICG@ZIF-8-DOX@MNs. Besides, the color of needle tips transformed to red after nanoparticle loading, implying the successful accumulation of nanoparticles into the needle cavity. To further confirm the distribution of MIL-88-ICG@ZIF-8-DOX in the MNs, the MNs were imaged by CLSM in both vertical- and base-sectional view. As shown in Fig. 5B, the nanoparticles were mainly encapsulated in the needles with a homogenous distribution and no extra nanoparticles appeared in the base. Furthermore, the distribution of red fluorescence (DOX) was identified with the green fluorescence (ICG), indicating that nanocarrier breakdown or premature drug release did not occur during the fabrication process of MNs. Three-dimensional modelling was introduced to match the overall distribution in Fig. 5C. The cross-sectional view of MNs in various height was displayed in Supporting Information Fig. S8, further confirming the homogenous fluorescent distribution. These results demonstrated that the MIL-88-ICG@ZIF-8-DOX nanoparticles were successfully concentrated in the needle tips of MNs and the process of MNs fabrication had negligible influence on the fluorescent stability of nanoparticles.

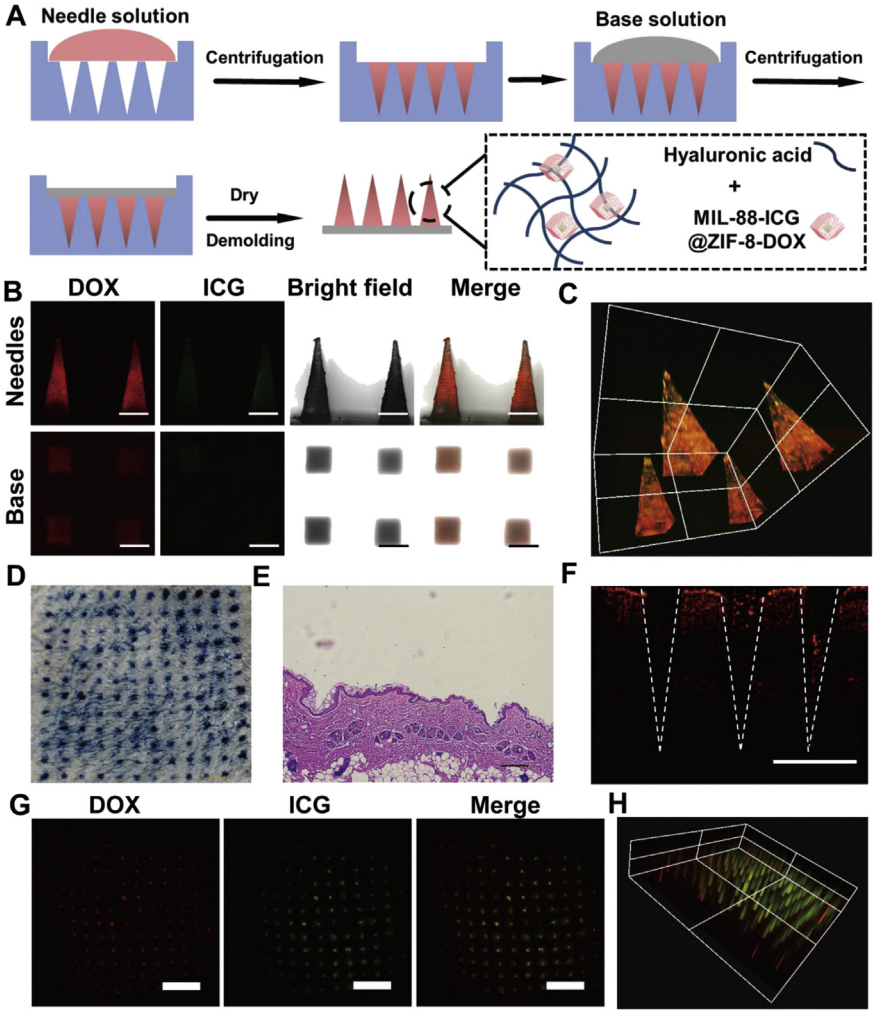


**Figure 5** (A) Schematic illustration of the fabrication process of MIL-88-ICG@ZIF-8-DOX@MNs (B) CLSM images of MIL-88-ICG@ZIF-8-DOX@MNs from the vertical- and base-sectional view (scale bar: 300 μm) (C) Three-dimensional modelling of MIL-88-ICG@ZIF-8-DOX@MNs *via* CLSM (D) The rat skin inserted by MIL-88-ICG@ZIF-8-DOX@MNs and followed by trypan blue staining (scale bar: 1.5 mm) (E) H&E staining section of rat skin after insertion (scale bar: 100 μm) (F) OCT image of rat skin after application of MNs (scale bar: 500 μm) (G) CLSM images of skin tissue after administration (scale bar: 2 mm) and (H) the relevant three-dimensional modelling image.

Successful skin insertion of MNs is the key factor for the transdermal drug delivery. Fig. 5D was the photograph of pierced skin stained by trypan blue solution. The obvious blue spots were in corresponding to the puncture site of MNs tips. The skin penetration capability was further evidenced by H&E and OCT, which revealed the obvious destruction of corneum barrier (Fig. 5E and F). The results of H&E also reflected that no visible inflammation such as neutrophil infiltration was induced by MNs. Compared with the corresponding skin insertion results of HA microneedles (Supporting Information Fig. S9–S11), the introduction of nanoparticles in the needles showed negligible effect on mechanical strength of MNs. Fig. 5G was the skin tissue observed by CLSM from the cross-sectional view and Fig. 5H was skin overall modeling by the three dimension imaging technology. The residual fluorescence in the skin tissue illustrated that the nanoparticles can be delivered and retained to the skin even after the base patch was removed, which is the premise for combinational treatment. The transient microchannels in the skin quickly recovered 3 h post MNs administration (Supporting Information Fig. S12).

Additionally, the *in vitro* photothermal ability of MIL-88-ICG@ZIF-8-DOX@MNs was studied to determine whether the fabrication process of MNs had influence on the photothermal ability of MIL-88-ICG@ZIF-8-DOX. The results in Supporting Information Figs. S13 and S14 both confirmed that the nanoparticles presented remarkable photothermal ability even after fabricated into MNs.

### 3.6. *In vivo antitumor activity*

To further verify the antitumor therapeutic efficacy, tumor model was established by implanting $1 \times 10^7$ 4T1 cells at the back of mice and kept feeding until the tumor volume reached approximately 100 $mm^3$. The tumor-bearing mice were randomly divided into eight groups with the following treatments: (1) control group (Control), (2) intravenous injection of MIL-88-ICG@ZIF-8-DOX + NIR (i.v.+NIR), (3) intratumoral injection of MIL-88-ICG@ZIF-8-DOX + NIR (i.t.+NIR), (4) MIL-88@ZIF-8-DOX@MNs (D@MNs), (5) MIL-88-ICG@ZIF-8@MNs + NIR (I@MNs + NIR), (6) MIL-88-ICG@ZIF-8-DOX@MNs

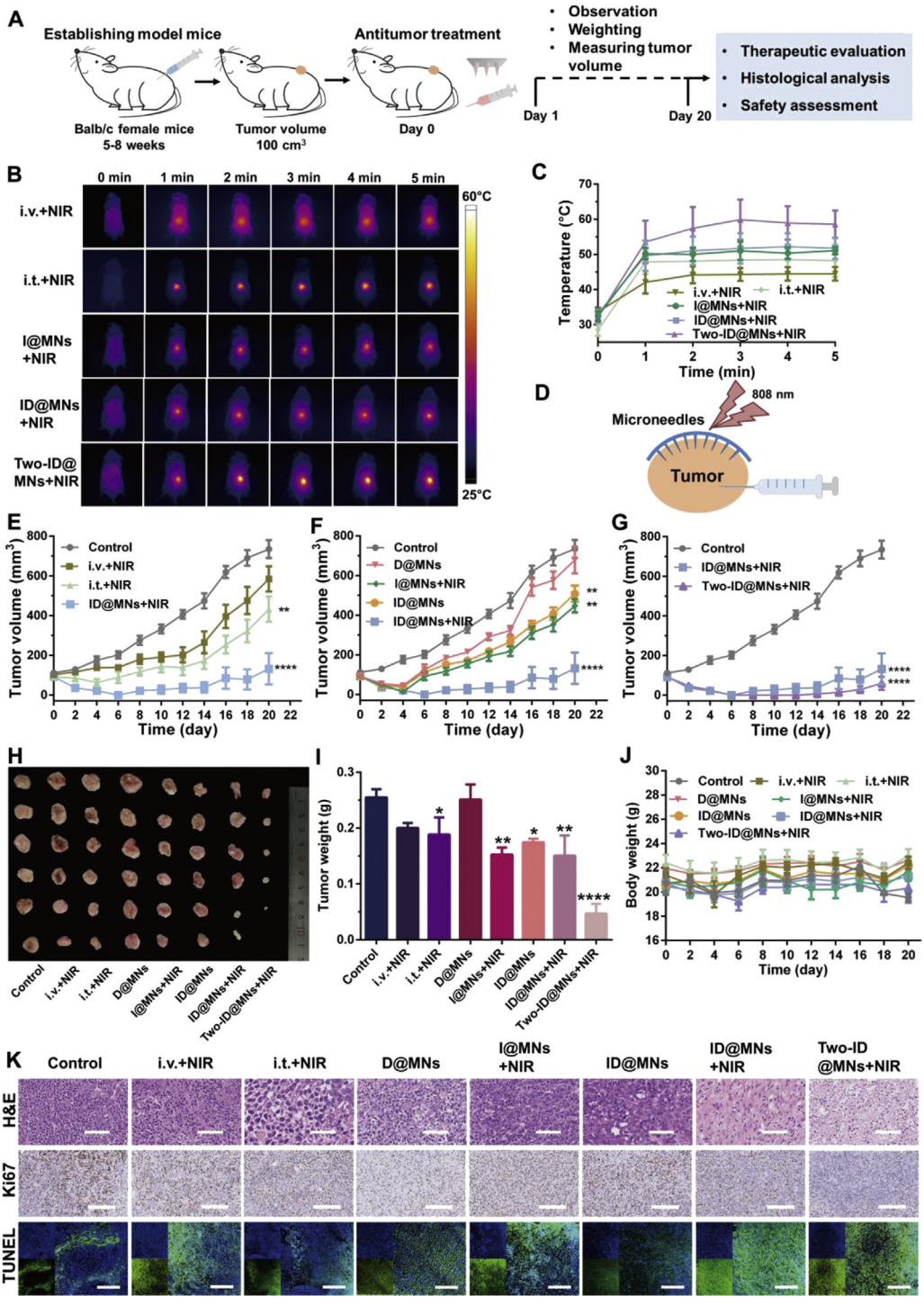


**Figure 6** (A) Schematic illustration of *in vivo* antitumor experimental outline (B) The thermographic images of mice and (C) the corresponding local temperature change curve in NIR treated groups (mean ± SD, $n = 6$) (D) Schematic illustration of administration methods (MNs and intratumoral injection) (E−G) Tumor volume growth curve of different groups for 20 days (mean ± SD, $n = 6$) (H) Photographs of tumors excised from different treated groups at Day 20 (I) Tumor weight of tumor-bearing mice after different treatments (mean ± SD, $n = 6$). $^{*}P < 0.05$ *vs.* Control; $^{**}P < 0.01$ *vs.* Control; $^{***}P < 0.001$ *vs.* Control; $^{****}P < 0.0001$ *vs.* Control (J) Body weight of tumor-bearing mice for 20 days (mean ± SD, $n = 6$) (K) Tumor section analysis by H&E staining (scale bar: 100 μm), Ki67 staining (scale bar: 150 μm), and TUNEL staining (scale bar: 200 μm).

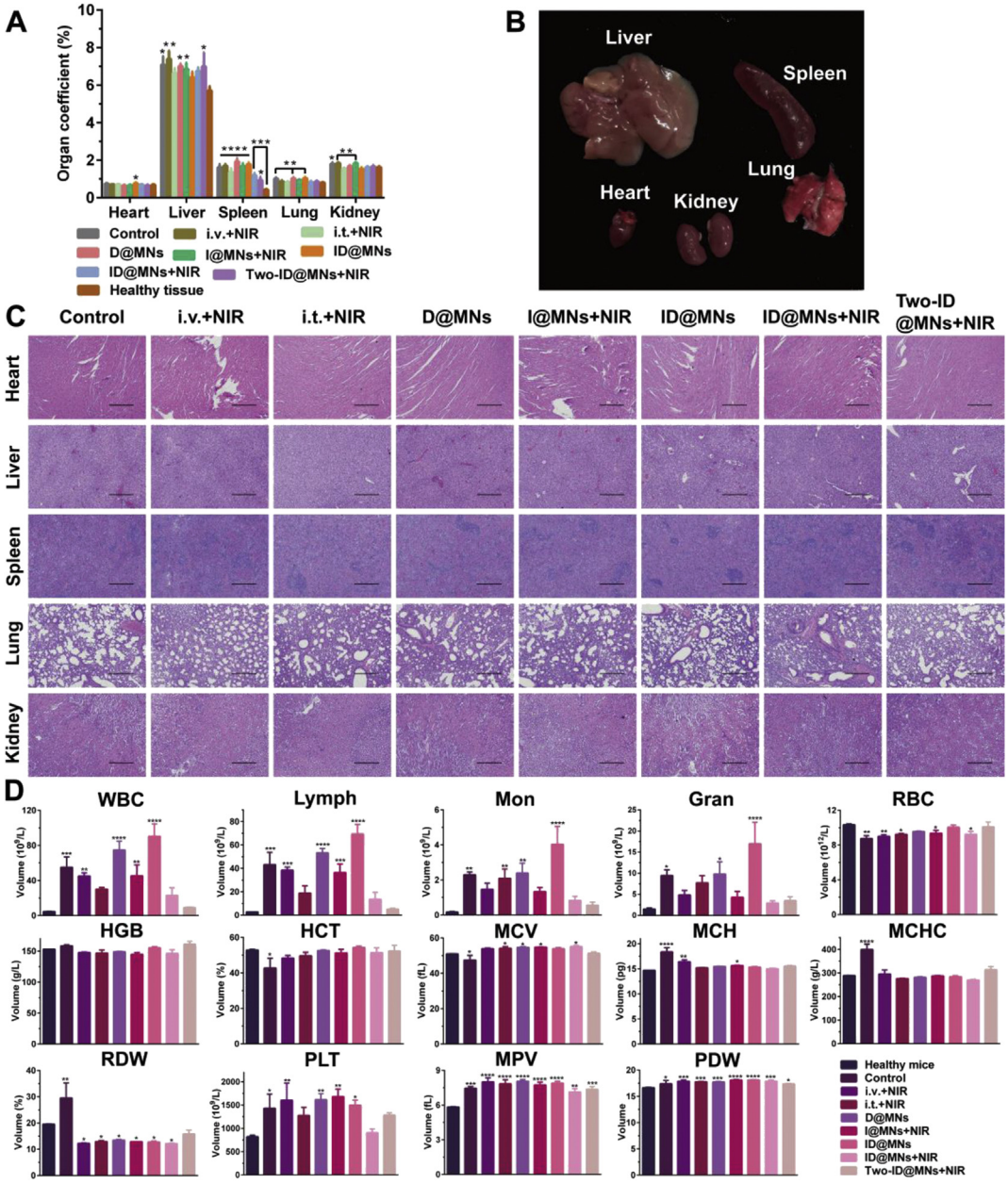


**Figure 7** (A) The weight coefficient index of organs from healthy mice and tumor-bearing mice after various treatments (mean ± SD, $n = 6$). $^{*}P < 0.05$ *vs.* healthy tissue; $^{**}P < 0.01$ *vs.* healthy tissue; $^{***}P < 0.001$ *vs.* healthy tissue; $^{****}P < 0.0001$ *vs.* healthy tissue (B) Photograph of major organs in tumor-bearing mice (C) H&E-stained images of major organs sections (scale bar: 100 μm) and (D) blood routine examination of experimental mice (mean ± SD, $n = 3$). $^{*}P < 0.05$ *vs.* healthy mice; $^{**}P < 0.01$ *vs.* healthy mice; $^{***}P < 0.001$ *vs.* healthy mice; $^{****}P < 0.0001$ *vs.* healthy mice.

(ID@MNs), (7) MIL-88-ICG@ZIF-8-DOX@MNs + NIR (ID@MNs + NIR), (8) two patches of MIL-88-ICG@ZIF-8-DOX@MNs + NIR (Two-ID@MNs + NIR). The administration schedule of *in vivo* antitumor study was presented in Fig. 6A.

Local hyperthermia, the key factor for PTT, can not only accelerate the drug release but also be beneficial for the Fenton reaction and the production of ROS[23]. Therefore, the *in vivo* photothermal effect of NIR-treated groups (i.v.+NIR, i.t.+NIR, I@MNs + NIR, ID@MNs + NIR, and Two-ID@MNs + NIR) were assessed by infrared thermal imaging (Fig. 6B) and the corresponding temperature change curve was presented in Fig. 6C. Under 808 nm laser irradiation, the local temperature increased steadily to approximately 50 °C as the irradiation time prolonged. Moreover, the local high temperature was concentrated precisely to the tumor region. Although the mice in the i.v.+NIR group received 5-fold higher dosage, the local temperature was the lowest, which indicated that a small number of nanoparticles reached the tumor site due to the systemic circulation. Besides, intratumoral injection did not present equal photothermal conversion effect compared with microneedle groups, which might be ascribed to the limited distribution of single injection (Fig. 6D).

The antitumor therapeutic effect was evaluated by measuring the relative tumor volume every two days. As shown in Fig. 6E, the tumor volume of control group increased rapidly and approximately 799% of the initial volume at Day 20. By contrast, the treated groups all exhibited tumor inhibition to some extent. For different administration routes, MNs patch (ID@MNs + NIR) showed significantly higher inhibition rate (82.1%) than intravenous injection (20.4%) and intratumoral injection (41.2%). Unlike the systemic circulation obstruction of intravenous injection, MNs can realize directly intratumoral administration with extremely effective accumulation. As compared with intratumoral injection, MNs provide multipoint-like injection due to the well-designed structure with several microscale drug-loaded tips, resulting in spatially uniform drug distribution and higher photothermal conversion. Therefore, compared with intravenous injection and intratumoral injection, MNs administration presented remarkable tumoricidal ability. As for various therapeutic systems, the results in Fig. 6F reflected the fact that the combination of photothermal/photodynamic/chemotherapy (ID@MNs + NIR) exhibited superior tumor suppression effect in comparison with the single chemotherapy group 7.6% and the PTT group 39.0%. In addition, improving the initial administrated dosage was also benefit for inhibiting cancer cells (Fig. 6G).

To further evaluate the antitumor efficiency, all the mice were sacrificed on Day 20 with the tumor tissues collected and weighted (Fig. 6H and I). The histogram of tumor weight was consistent with the curve of tumor size, indicating the remarkable tumor suppression ability of ID@MNs + NIR. The H&E staining section of tumor tissues showed that different apoptotic and necrotic levels were observed in treated groups (Fig. 6K), which indicated the content of dead cells[43]. The most obvious atypia of cancer cells were presented in the group of Two-ID@MNs + NIR with aggravated cell necrosis, detectable atypia of nucleus, and inferior dyeing of chromatin. Ki-67 was an indicator related to the proliferation capacity of cells. The control group presented the rapid cell proliferation while efficient proliferation inhibition was found in Two-ID@MNs + NIR group. Furthermore, the apoptotic cells were detected by TUNEL staining, further verifying the combinational therapeutic efficacy.

The body weight of mice during the whole treatment was monitored to evaluate the biocompatibility of the drug delivery system. As shown in Fig. 6J, no significant change was exhibited in all groups, demonstrating the negligible toxicity of MIL-88-ICG@ZIF-8-DOX. In addition, all the major organs and blood were collected for safety assessment. As shown in Fig. 7A, no noticeable weight change was discerned in the major organs (heart, liver, lung, and kidney) except for the spleen as compared with the healthy mice. This is because that the tumor-bearing mice all catch splenomegaly (Fig. 7B), which was consistent with the previous research[44]. H&E staining for major organs were exhibited in Fig. 7C. Compared with healthy mice, no obvious abnormities, such as fibrosis, infiltration, and inflammation were observed in the treated mice. The related blood routine examination of all groups was displayed in Fig. 7D. The hematology markers in the synergistic groups showed no physiologically significant differences in comparison with the healthy mice, suggesting no hemolytic anemia, acute infection or bone marrow dysfunction occurred in the synergistic groups.

## 4. Conclusion

In this study, a synergistic photothermal/photodynamic/chemotherapy multimodal antitumor system was successfully constructed based on core–shell dual metal–organic frameworks. The unique structure of the nanocarrier not only endowed it two individual functional zones for various drug co-delivery, but also generated adequate oxygen for PDT treatment *via* Fenton-like reaction. This novel self-propulsion system possessed remarkable ability to deliver and protect cargos and realize site- and time-specific controlled release. Moreover, the *in vivo* study further confirmed an effective, safe, and precise antitumor behavior. With further optimization and in-depth study, we believe such a photothermal/photodynamic/chemotherapy synergistic system will be a powerful weapon for antitumor treatment with superior efficacy.

## Acknowledgments

This work was supported by the National Nature Science Foundation of China (Grant Nos. 81773660 and 81803466), the Research and Development Plan for Key Areas in Guangdong Province (Grant No. 2019B020204002, China), and Natural Science Foundation of Guangdong Province (Grant No. 2018A030310095, China).

## Author contributions

Biyuan Wu designed and carried out the research, performed data collecting and wrote the manuscript. Jintao Fu, Yinting Zhao participated part of the experiments. Yixian Zhou and Sulan Luo performed data analysis. Guilan Quan revised the manuscript. Xin Pan and Chuanbin Wu supervised the project. All of the authors have read and approved the final manuscript.

## Conflicts of interest

The authors have no conflict of interest to declare.

## Appendix A. Supporting information

Supporting data to this article can be found online at https://doi.org/10.1016/j.apsb.2020.07.025.

## References

1. Bray F, Ferlay J, Soerjomataram I, Siegel RL, Torre LA, Jemal A. Global cancer statistics 2018: GLOBOCAN estimates of incidence and mortality worldwide for 36 cancers in 185 countries. *CA Cancer J Clin* 2018;**68**:394–424.
2. Lucky SS, Soo KC, Zhang Y. Nanoparticles in photodynamic therapy. *Chem Rev* 2015;**115**:1990–2042.
3. Ma Z, Jia X, Bai J, Ruan Y, Wang C, Li J, et al. $MnO_2$ gatekeeper: an intelligent and $O_2$-evolving shell for preventing premature release of high cargo payload core, overcoming tumor hypoxia, and acidic $H_2O_2$-sensitive MRI. *Adv Funct Mater* 2017;**27**:1604258.
4. Chen C, Ou H, Liu R, Ding D. Regulating the photophysical property of organic/polymer optical agents for promoted cancer phototheranostics. *Adv Mater* 2020;**32**:e1806331.
5. Liu R, Hu C, Yang Y, Zhang J, Gao H. Theranostic nanoparticles with tumor-specific enzyme-triggered size reduction and drug release to perform photothermal therapy for breast cancer treatment. *Acta Pharm Sin B* 2019;**9**:410–20.
6. Ni X, Zhang X, Duan X, Zheng HL, Xue XS, Ding D. Near-infrared afterglow luminescent aggregation-induced emission dots with ultrahigh tumor-to-liver signal ratio for promoted image-guided cancer surgery. *Nano Lett* 2019;**19**:318–30.

7. Chen C, Ni X, Jia S, Liang Y, Wu X, Kong D, et al. Massively evoking immunogenic cell death by focused mitochondrial oxidative stress using an AIE luminogen with a twisted molecular structure. *Adv Mater* 2019;**31**:1904914.
8. Zeng JY, Zhang MK, Peng MY, Gong D, Zhang XZ. Porphyrinic metal-organic frameworks coated gold nanorods as a versatile nanoplatform for combined photodynamic/photothermal/chemotherapy of tumor. *Adv Funct Mater* 2018;**28**:1705451.
9. Liu R, Xiao W, Hu C, Xie R, Gao HL. Theranostic size-reducible and no donor conjugated gold nanocluster fabricated hyaluronic acid nanoparticle with optimal size for combinational treatment of breast cancer and lung metastasis. *J Control Release* 2018;**278**:127−39.
10. Liu R, An Y, Jia WF, Wang YS, Wu Y, Zhen YH, et al. Macrophage-mimic shape changeable nanomedicine retained in tumor for multimodal therapy of breast cancer. *J Control Release* 2020;**321**:589−601.
11. Wang D, Zhou J, Shi R, Wu H, Chen R, Duan B, et al. Biodegradable core−shell dual-metal-organic-frameworks nanotheranostic agent for multiple imaging guided combination cancer therapy. *Theranostics* 2017;**7**:4605−17.
12. Sheng Z, Hu D, Zheng M, Zhao P, Liu H, Gao D, et al. Smart human serum albumin−indocyanine green nanoparticles generated by programmed assembly for dual-modal imaging-guided cancer synergistic phototherapy. *ACS Nano* 2014;**8**:12310−22.
13. Zhang H, Li Q, Liu R, Zhang X, Li Z, Luan Y. A versatile prodrug strategy to *in situ* encapsulate drugs in MOF nanocarriers: a case of cytarabine−IR820 prodrug encapsulated ZIF-8 toward chemo-photothermal therapy. *Adv Funct Mater* 2018;**28**:1802830.
14. Gao ST, Zheng PK, Li ZH, Feng XC, Yan WX, Chen SZ, et al. Biomimetic $O_2$-evolving metal-organic framework nanoplatform for highly efficient photodynamic therapy against hypoxic tumor. *Biomaterials* 2018;**178**:83−94.
15. Li X, Xing L, Hu Y, Xiong Z, Wang R, Xu X, et al. An RGD-modified hollow silica@Au core/shell nanoplatform for tumor combination therapy. *Acta Biomater* 2017;**62**:273−83.
16. Li Z, Hu Y, Howard KA, Jiang T, Fan X, Miao Z, , et alBesenbacher M Yu. Multifunctional bismuth selenide nanocomposites for antitumor thermo-chemotherapy and imaging. *ACS Nano* 2016;**10**:984−97.
17. Wu MX, Yang YW. Metal-organic framework (MOF)-based drug/cargo delivery and cancer therapy. *Adv Mater* 2017;**29**:1606134.
18. Wu BY, Fu JT, Zhou YX, Wang J, Feng XQ, Zhao YT, et al. Metal-organic framework-based chemo-photothermal combinational system for precise, rapid, and efficient antibacterial therapeutics. *Pharmaceutics* 2019;**11**:463.
19. Wang S, McGuirk CM, d'Aquino A, Mason JA, Mirkin CA. Metal-organic framework nanoparticles. *Adv Mater* 2018;**30**:e1800202.
20. Ma M, Bétard A, Weber I, Al-Hokbany NS, Fischer RA, Metzler-Nolte N. Iron-based metal-organic frameworks MIL-88B and $NH_2$-MIL-88B: high quality microwave synthesis and solvent-induced lattice "breathing". *Cryst Growth Des* 2013;**13**:2286−91.
21. Mellot-Draznieks C, Serre C, Surble S, Audebrand N, Férey G. Very large swelling in hybrid frameworks: a combined computational and powder diffraction study. *J Am Chem Soc* 2005;**127**:12273−85.
22. Horcajada P, Serre C, Maurin G, Ramsahye NA, Balas F, Vallet-Regí M, et al. Flexible porous metal-organic frameworks for a controlled drug delivery. *J Am Chem Soc* 2008;**130**:6774−80.
23. Wang P, Shi Y, Zhang S, Huang X, Zhang J, Zhang Y, et al. Hydrogen peroxide responsive iron-based nanoplatform for multimodal imaging-guided cancer therapy. *Small* 2019;**15**:e1803791.
24. Lismont M, Dreesen L, Wuttke S. Metal-organic framework nanoparticles in photodynamic therapy: current status and perspectives. *Adv Funct Mater* 2017;**27**:1606314.
25. Sakamaki Y, Ozdemir J, Heidrick Z, Watson O, Shahsavari HR, Fereidoonnezhad M, et al. Metal-organic frameworks and covalent organic frameworks as platforms for photodynamic therapy. *Comments Mod Chem* 2019;**38**:238−93.
26. Hu F, Mao D, Kenry, Wang Y, Wu W, Zhao D, et al. Metal-organic framework as a simple and general inert nanocarrier for photosensitizers to implement activatable photodynamic therapy. *Adv Funct Mater* 2018;**28**:1707519.
27. Wang TZ, Li SQ, Zou Z, Hai L, Yang X, Jia X, et al. A zeolitic imidazolate framework-8-based indocyanine green theranostic agent for infrared fluorescence imaging and photothermal therapy. *J Mater Chem B* 2018;**6**:3914−21.
28. Yang C, Xu J, Yang DD, Wang XX, Liu B, He NY, et al. ICG@ZIF-8: one-step encapsulation of indocyanine green in ZIF-8 and use as a therapeutic nanoplatform. *Chin Chem Lett* 2018;**29**:1421−4.
29. Liu YL, Zhao XJ, Yang XX, Li YF. A nanosized metal-organic framework of Fe-MIL-88$NH_2$ as a novel peroxidase mimic used for colorimetric detection of glucose. *Analyst* 2013;**138**:4526−31.
30. Hou AL, Quan GL, Yang BB, Lu C, Chen ML, Yang D, et al. Rational design of rapidly separating dissolving microneedles for precise drug delivery by balancing the mechanical performance and disintegration rate. *Adv Healthcare Mater* 2019;**8**:1900898.
31. Lin SQ, Quan GL, Hou AL, Yang PP, Peng TT, Gu YK, et al. Wu. Strategy for hypertrophic scar therapy: improved delivery of triamcinolone acetonide using mechanically robust tip-concentrated dissolving microneedle array. *J Control Release* 2019;**306**:69−82.
32. Song Z, Qiu F, Zaia EW, Wang Z, Kunz M, Guo J, et al. Dual-channel, molecular-sieving core/shell ZIF@MOF architectures as engineered fillers in hybrid membranes for highly selective $CO_2$ separation. *Nano Lett* 2017;**17**:6752−8.
33. Ranji-Burachaloo H, Fu Q, Gurr PA, Dunstan DE, Qiao GG. Improved Fenton therapy using cancer cell hydrogen peroxide. *Aust J Chem* 2018;**71**:826.
34. Wang L, Guan H, Wang Z, Xing Y, Zhang J, Cai K. Hybrid mesoporous-microporous nanocarriers for overcoming multidrug resistance by sequential drug delivery. *Mol Pharm* 2018;**15**:2503−12.
35. Kuo CH, Tang Y, Chou LY, Sneed BT, Brodsky CN, Zhao Z, et al. Yolk-shell nanocrystal@ZIF-8 nanostructures for gas-phase heterogeneous catalysis with selectivity control. *J Am Chem Soc* 2012;**134**:14345−8.
36. Xu F, Liu M, Li X, Xiong Z, Cao X, Shi X, et al. Loading of indocyanine green within polydopamine-coated laponite nanodisks for targeted cancer photothermal and photodynamic therapy. *Nanomaterials* 2018;**8**:347.
37. Anand R, Borghi F, Manoli F, Manet I, Agostoni V, Reschiglian P, et al. Host−guest interactions in Fe(III)−trimesate MOF nanoparticles loaded with doxorubicin. *J Phys Chem B* 2014;**118**:8532−9.
38. Ranji-Burachaloo H, Karimi F, Xie K, Fu Q, Gurr PA, Dunstan DE, et al. MOF-mediated destruction of cancer using the cell's own hydrogen peroxide. *ACS Appl Mater Interfaces* 2017;**9**:33599−608.
39. Chen WH, Luo GF, Vazquez-Gonzalez M, RCazelles, Sohn YS, Nechushtai R, et al. Glucose-responsive metal-organic-framework nanoparticles act as "smart" sense-and-treat carriers. *ACS Nano* 2018;**12**:7538−45.
40. Dong K, Wang Z, Zhang Y, Ren J, Qu X. Metal-organic framework-based nanoplatform for intracellular environment-responsive endo/lysosomal escape and enhanced cancer therapy. *ACS Appl Mater Interfaces* 2018;**10**:31998−2005.
41. Sun ZJ, Jiang JZ, Li YF. A sensitive and selective sensor for biothiols based on the turn-on fluorescence of the Fe-MIL-88 metal-organic frameworks-hydrogen peroxide system. *Analys* 2015;**140**:8201−8.
42. Cheng H, Zhu JY, Li SY, Zeng JY, Lei Q, Chen KW, et al. An $O_2$ self-sufficient biomimetic nanoplatform for highly specific and efficient photodynamic therapy. *Adv Funct Mater* 2016;**26**:7847−60.
43. Yang JC, Chen Y, Li YH, Yin XB. Magnetic resonance imaging-guided multi-drug chemotherapy and photothermal synergistic therapy with pH and NIR-stimulation release. *ACS Appl Mater Interfaces* 2017;**9**:22278−88.
44. Li YT, Jin J, Wang DW, Lv JW, Hou K, Liu YL, et al. Coordination-responsive drug release inside gold nanorod@metal-organic framework core−shell nanostructures for near-infrared-induced synergistic chemo-photothermal therapy. *Nano Res* 2018;**11**:3294−305.